Article

Human Exhalation CO_2 Sensor Based on the PEI-PEG/ZnO/NUNCD/Si Heterojunction Electrode

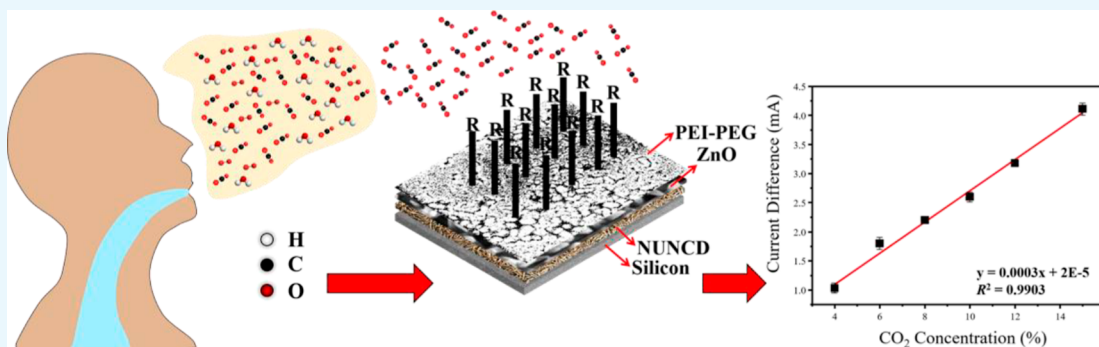Ching Chang, Chi-Young Lee, and Nyan-Hwa Tai*

Read Online

ACCESS | Metrics & More | Article Recommendations | Supporting Information

ABSTRACT: Gas sensors based on semiconductors have outstanding sensitivity compared with the oxide-based devices; however, the high operation temperature greatly hinders its development in practical applications. Chronic obstructive pulmonary disease (COPD) is one of the leading causes of death worldwide, and the patients with severe COPD with or without exacerbation tend to have airflow obstruction, which results in an increase of CO_2 concentration and subsequent hypercapnic respiratory failure. At present, COPD detection relies on professional operation; however, the patients suffer great discomfort during the arterial blood sampling. All these facts reduce patient's willingness to test their physical health. Thus, noninvasive monitoring of CO_2 levels is crucial for the early diagnosis of high-risk COPD patients. A nitrogen-incorporated ultrananocrystalline diamond (NUNCD) film exhibits excellent properties in biosensing and polyetherimide-polyethylene glycol (PEI-PEG) polymer possesses a great capability of CO_2 capturing. By incorporating NUNCD into PEI-PEG film, this work focuses on ameliorating the sensitivity and selectivity of the present semiconductor CO_2 sensor. From the theoretical regression analyses of the experimental results, it is found that the excellent performance of the PEI-PEG/ZnO/NUNCD/Si electrode is contributed by two main reaction layers, the adsorption layer (PEI-PEG) and the electric transfer layer (ZnO/NUNCD). The selectivity is dominated by the PEI-PEG adsorption layer and the sensitivity is directly related to the changes in the work function of the ZnO/NUNCD interface. The high aspect ratio (>10) of the flower-like ZnO structure, growth from ZnO nanoparticles, can provide a more active adsorption area, as a result, extremely enhancing the sensitivity of the CO_2 sensor.

■ INTRODUCTION

Nowadays, for better welfare, sensors, such as glucose sensor,[1] projectile sensor,[2] liquid petroleum gas sensor,[3] and gas sensor,[4−6] developed for various applications are indispensable. Regarding the clinical diagnosis based on exhalation, patients with chronic obstructive pulmonary disease (COPD), one of the top five chronic diseases in the world,[7] have a lower oxygen utilization rate than healthy people, implying that the CO_2 concentrations in the exhalations of COPD patients and healthy people are different. COPD is characterized by chronic airway inflammation resulting from persistent toxic gases such as cigarette smoke, which causes excessive oxidative stress, cytokine and chemotactic factor release, and inflammatory cell recruitment in the airways. This is followed by increased production of proteases such as matrix metalloproteinase,[8,9] which may induce the loss of elastic recoil and destruction of

parenchymal tissue, resulting in the early collapse of small airways and hyperinflation called emphysema.[10,11] To alleviate the reliance of symptom assessment on invasive medical treatments,[12] the use of tidal breath analysis as a building block to design devices for detecting CO_2 levels from exhaled breath is essential. The difficulty of COPD symptom detection presently lies in professional operation, and the patients suffer from significant discomfort during the arterial puncture sampling,[13−16] all of which lower their willingness to have
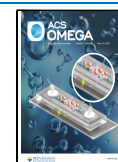
their medical examination. Therefore, CO_2 gas sensing with a simple and noninvasive process has become an important issue for COPD patients requiring immediate medical assistance. In this regard, a simple CO_2 sensing device would greatly alleviate the gap in monitoring the disease severity and the risk of respiratory failure in COPD patients and provide a useful tool for clinical practice. At present, there is a commercial CO_2 measurement technique called capnography which provides physiological information based on infrared spectroscopy. However, COPD sensing based on infrared light adsorption is highly susceptible to CO_2 in the atmosphere, and thus the procedure must be performed under tracheal intubation conditions.

Traditionally, devices based upon metal-oxides have been used to sense CO_2 gas. However, the high operating temperature and high fabrication cost of the devices are disadvantageous of the metal-oxides-based devices for wide applications.[17] For semiconductor materials like $CuO-BaTiO_3$, the high operation temperature remains an obstacle.[18] La_2O_3 also has a higher cost than common metal oxide materials such as ZnO, Fe_2O_3, and TiO_2.[19] Thus, for sensing purposes, ZnO is expected to be more appropriate owing to its excellent electrical properties, low cost, large surface-to-volume ratio, reliable performance, and wide band gap (3.37 eV), making ZnO widely applicable for device applications such as gas sensing, photodetectors, field emitters, and solar cells.[20−25] However, the ZnO-based CO_2 sensor can only operate at high temperatures,[26] and this obstacle can be overcome through the design of a structure with improved electron transmission efficiency.[27−29] Carbon nanomaterials have different microstructures for various applications, for example, if the hydrophilicity property is of concern, graphene oxides (GO) could be a good starting material to approach;[30] on the other hand, if a high electrical conductance property is required, carbon nanotubes (CNTs), reduced graphene oxide (rGO), and nitrogen-doped ultrananocrystalline diamond (NUNCD) are the most promising candidates.

According to the published articles, it was reported that the incorporation of N_2 into the CH_4 plasma in the UNCD fabrication process can synthesize electrically active acicular-shaped NUNCD which possesses excellent charge transmission properties with high surface area.[31,32] In particular, nitrogen-incorporated diamond films can increase the formation of sp^2 hybridization, which is beneficial in increasing the number of charge carriers.[33] NUNCDs have been used in several applications, especially in biosensors;[34−36] in this regard, the sensing surface area and the electrical conductivity are two key parameters to affect the sensor performance. A heterojunction semiconductor system can create more electron travel pathways due to the generation of electric fields at the interfaces.[37−40] NUNCD and ZnO/NUNCD on the Si substrate possess different work functions; the lower work function of ZnO/NUNCD facilitates carrier transfer through the interfaces.

Therefore, ZnO and NUNCD are integrated for fabricating the high-performance CO_2 sensor in this study. In the ZnO/NUNCD/Si hybrid structure, the interface between ZnO and NUNCD provides favorable routes for charge transport, while the NUNCD surface, containing numerous peaks and valleys resulting in high surface area, enhances the response of the sensing device. To the best of our knowledge, no effort has been made to use ZnO and NUNCD as the building blocks for the fabrication of high-sensitivity gas sensors, especially for

inert CO_2. Thus, the heterojunction structure was designed and used as the main conductive layer for CO_2 sensing. In addition, a polyethylenimine (PEI) and polyethylene glycol (PEG) blend was used as an adsorption layer to improve the selectivity of the CO_2 sensing devices.[41] PEI is particularly effective to capture CO_2 because of its amine-rich groups and low molecular weight,[42,43] while PEG can adsorb water molecules from the environment because of the presence of hydroxyl groups. Adsorption of more water molecules can enhance the Le Chatelier principle reaction, as a result, magnifying the electrical signal. Furthermore, the participation of water molecules during CO_2 adsorption can also improve the sensitivity because of the presence of protonation.[44] According to the design, the prepared devices exhibited excellent sensitivity at room temperature. Systematic investigations reveal that the as-fabricated PEI-PEG/ZnO/NUNCD/Si electrode is a promising design for a CO_2 sensor that can overcome the deficiencies of the high operating temperature of the current semiconductor-type CO_2 gas sensor.

■ EXPERIMENTAL SECTION

In the process for NUNCD film fabrication, a 0.5×0.5 cm^2 Si(100) substrate was first ultrasonicated in a methanol solution containing the nanodiamond powder (FACT, UDD-90, 5−10 nm) and titanium powder (Alfa Aesar, 99%, 325 mesh). Some of the particle fragments were implanted and served as heterogeneous nucleation sites for initial grain growth. The substrate was then loaded into a chamber and treated using a hydrogen/argon (50% + 50%) plasma for 10 min to remove surface contaminants such as native SiO_2 before NUNCD growth. For the growth of a NUNCD film, the plasma containing 94% nitrogen and 6% methane was applied for 60 min, and the power and pressure were controlled to be 1400 W and 35 Torr, respectively. In addition, an electric field bias of −300 V was applied to pull the plasma sphere downward such that the sample was exposed at its center and experienced a more homogeneous plasma environment.[25]

The ZnO/NUNCD/Si and ZnO/Si composite electrodes were prepared by the coprecipitation of flower-like ZnO on the NUNCD/Si surface and pristine Si substrate, respectively. Coprecipitation is a convenient and simple method for incorporating metal-oxide nanostructures on thin-film substrates. The flower-like ZnO was deposited on the upside-down NUNCD/Si surface by coprecipitation, which was carried out in a fresh aqueous solution of 0.08 M $Zn(CH_3COO)_2$ and 1 M NaOH at 50 °C for 1 h.

For the preparation of the PEI-PEG blend, PEI and PEG with 1.0 wt % each were dissolved in isopropanol. After 10 min of ultrasonication of the mixture, 10 mL of the blended solution was sprayed onto the ZnO/NUNCD/Si surface. Because of PEI-PEG coating, the flower-like ZnO structure can be retained during the subsequent handling, fabrication, and operation.

For the analyses of the PEI-PEG/ZnO/NUNCD/Si samples, the $I-V$ curves and CO_2 sensing properties of the films were measured using a Keithley 2410 source meter at ambient temperature. The crystallinity was examined using an X-ray diffractometer (XRD, Bruker D2 PHASER) in the scattering range of 30−75° at a scanning rate of 0.02°/s. The work function was studied by X-ray photoelectron spectroscopy (ULVAC-PHI PHI Quantera II) employing a UV source of He I (21.22 eV). In addition, the surface morphology and

cross-sectional view of the films were characterized using field emission scanning electron microscopy (FESEM, Hitachi SU8010). Further details on the ZnO structure and elemental analysis were obtained via transmission electron microscopy/ corrected spherical aberration scanning transmission electron microscopy (TEM/Cs-STEM, ARM200FTH) with energy-dispersive X-ray spectroscopy (EDS, Oxford MAX80) at an acceleration voltage of 200 V. The STEM images were acquired in both the annular bright-field (ABF) mode (collection angle 10−17 mrad) and high-angle annular dark-field (HAADF) mode (collection angle 68−175 mrad) by scanning a probe with a convergence angle of 22 mrad. All the TEM/Cs-STEM samples were prepared using a focused ion beam (Hitachi NX2000).

RESULTS AND DISCUSSION

Figure 1 shows the XRD spectra of the ZnO/Si, NUNCD/Si, and ZnO/NUNCD/Si samples. The ZnO spectrum depicts
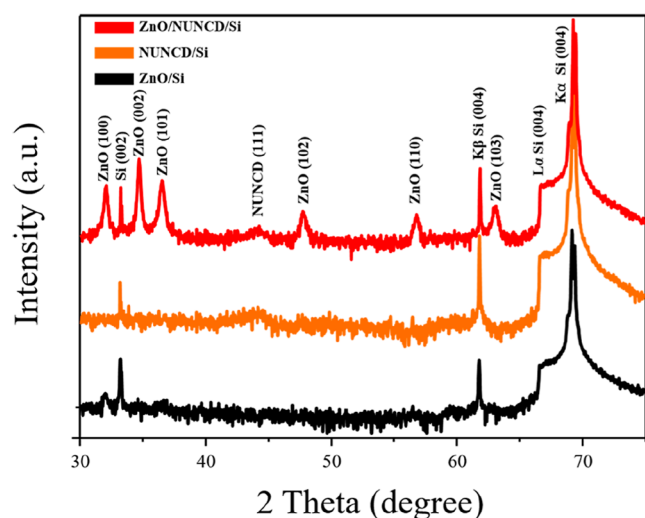
Figure 1. XRD spectra of ZnO/Si, NUNCD/Si, and ZnO/NUNCD/ Si.

the formation of the ZnO nanostructure with a hexagonal wurtzite phase (JCPDS card no. 36-1451) in the $P\bar{6}3/m$ space group. The synthesized ZnO structure on the silicon substrate shows only a ZnO (100) peak at approximately 31.80°, corresponding to a d-spacing of 2.814 Å. However, after the ZnO coating on the NUNCD film, additional peaks at 34.45, 36.29, 47.58, 56.65, and 62.91° were observed, which correspond to the polycrystalline structure of ZnO. The XRD spectra indicate that the NUNCD film provides nucleation sites for ZnO coating, confirming the successful preparation of a polycrystalline ZnO film.

The surface morphologies of NUNCD/Si, ZnO/NUNCD/ Si, and PEI-PEG/ZnO/NUNCD/Si are shown in Figure 2. With the typical acicular-shaped structure of NUNCD illustrated in Figure 2a,b, the images clearly depict that the acicular NUNCD has the size of a few tens of nanometers which is capable of providing numerous nucleation sites for ZnO growth. Without NUNCD, ZnO with sparse density can be observed, as shown in Figure S1. Figure 2c,d shows the surface morphologies with low and high magnification, respectively, of the as-grown ZnO film. Flower-like ZnO with a diameter of less than 200 nm is observed. After the NUNCD film was completely deposited with flower-like ZnO, the
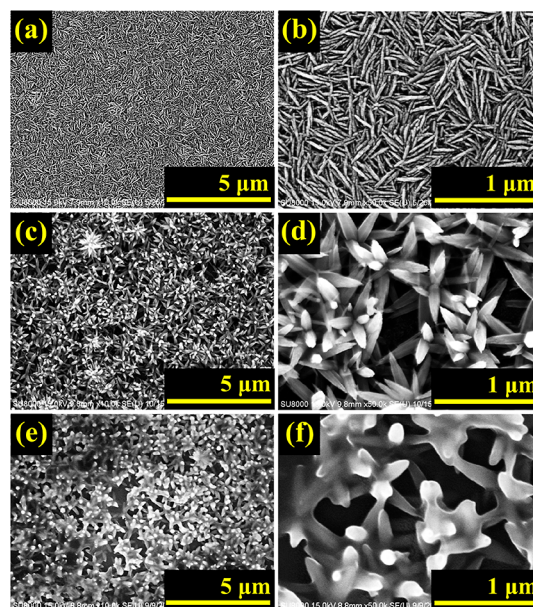

Figure 2. FESEM images of the top surfaces of (a,b) NUNCD/Si, (c,d) ZnO/NUNCD/Si, and (e,f) PEI-PEG/ZnO/NUNCD/Si.

specific surface area is significantly increased. To increase the CO_2 adsorption ability, a PEI-PEG layer was coated onto the ZnO/NUNCD/Si surface, as shown in Figure 2e,f. PEI has amine groups for adsorbing CO_2 and PEG has hydroxyl groups for capturing water molecules. The PEI-PEG layer is so thin that it can uniformly cover the flower-like ZnO surface while maintaining the ZnO topography. The PEI-PEG/ZnO/ NUNCD/Si electrode possesses higher sensitivity because of its inherent properties of higher surface area and better CO_2 adsorption capability. Additionally, the PEG can adsorb water molecules from the atmosphere, which can further improve the electrode response to carbon dioxide.

Figure 3a shows a schematic structure of the CO_2 sensing electrode. The electrode is composed of four parts: PEI-PEG (CO_2 adsorption layer), ZnO (surface area-promoting layer), NUNCD (nucleation site, conductive layer), and silicon (substrate). Besides, a TCNT layer was prepared to connect the electrode with the circuit. Figure 3b shows the I−V curves of PEI-PEG/ZnO/NUNCD/Si, ZnO/NUNCD/Si, NUNCD/ Si, and ZnO/Si. The linear I−V behavior of ZnO/NUNCD/Si confirmed the characteristic of good ohmic contact between the ZnO and NUNCD films. NUNCD/Si exhibited the best electrical conductivity of 0.18 Ω which is far better than that of the ZnO/Si (1210.12 Ω) sample. However, PEI-PEG/ZnO/ NUNCD/Si exhibited a moderate average resistance of 0.36 Ω, which indicates that even the PEI-PEG is an inherently nonconductive polymer, and the thin coating layer of the PEI-PEG layer insignificantly decreases the conductivity. The sensing process of the electrode can be illustrated using the schematic diagram of the device including the electrode and a circuit, as depicted in Figure 3c.

Figure 4a shows the cyclic current response of the PEI-PEG/ ZnO/NUNCD/Si electrode under the test at the conditions of 5.0% CO_2 and a constant voltage of 1.0 V. Three shutters were used to control the cyclic on, off, and pumping processes. First, the chamber was vacuumed to prevent pollution from the environment. Afterward, air was introduced into the chamber, which was used to simulate the electrode working in an atmospheric environment. Subsequently, 5% CO_2 was
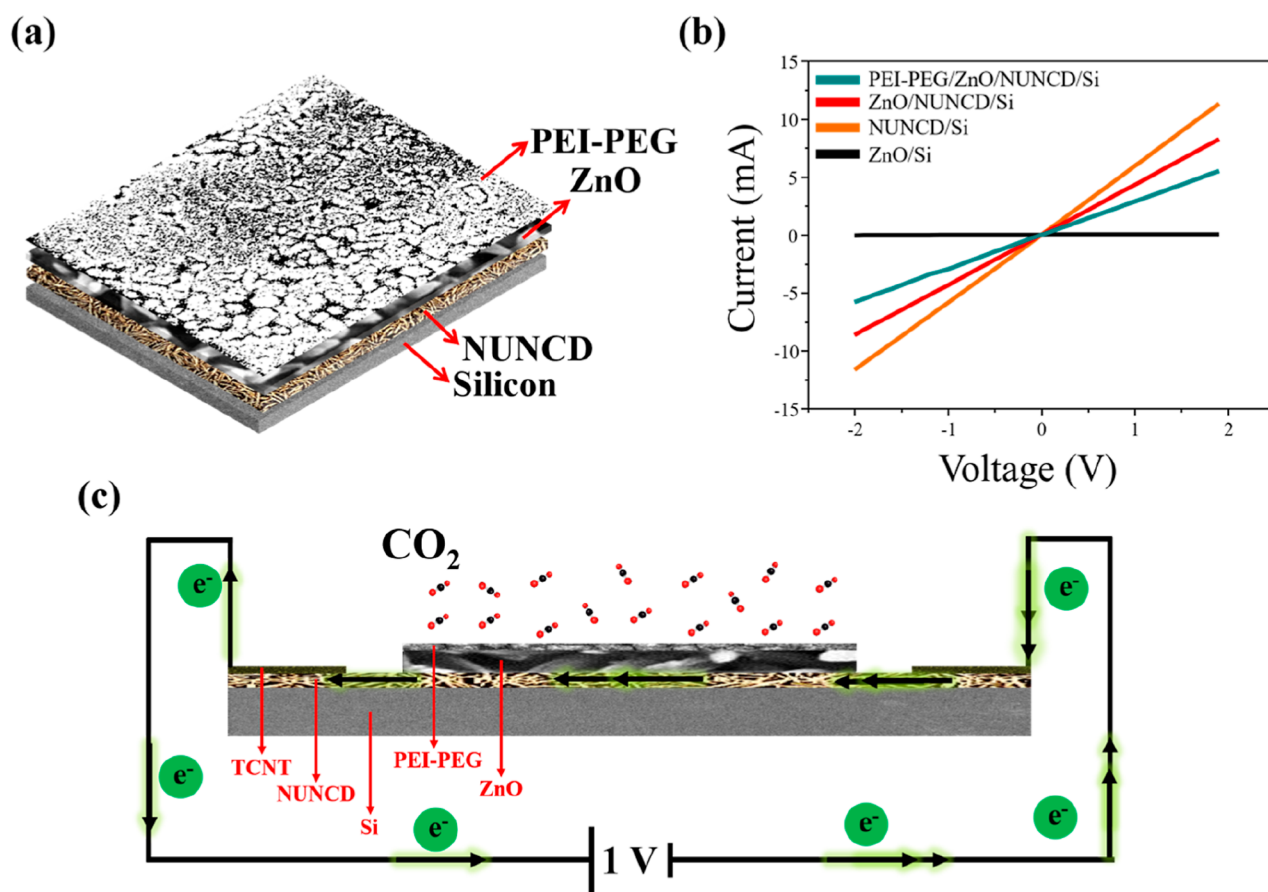
Figure 3. (a) Schematic diagram of the electrode structure, (b) $I-V$ characteristics of the different electrodes, and (c) schematic diagram of the sensing process.

channeled into the chamber; after the flow field reached a steady state, the test proceeded to the next cycle. The response of a heterojunction gas sensor is generally evaluated in terms of R, R_{Gas}, and ΔR, where R represents the initial current, R_{Gas} is the final current, and ΔR is the current difference $(R_{Gas} - R)$ of the electrode exposed to CO_2 gas. Excluding the first testing cycle, the average ΔR was approximately 0.004 mA, indicating that the electrode has excellent repeatability, as shown in Figure 4b. The system, including the acquisition computer, chamber, mass flow controller, pump, and gas cylinders, for testing the performance of the as-prepared electrode is schematically plotted in Figure 4c. The results show that the electrode is sensitive to CO_2 under atmospheric conditions because it exhibited identical responses under the same CO_2 concentration. The recovery time was fixed at 50 s by the pumping process after each testing cycle. In this study, the response time is defined as the time for the current to reach 90% of its maximum stable current. As shown in Figure 4a, the response time increased from 87 s of the 1st cycle to 124 s of the 8th cycle. Longer response time with the consecutive cyclic tests is due to detachment of the adhered residual CO_2 and water molecules on the electrode surface which originated from the CO_2 gas (with a relative humidity of 13%) in commercial gas cylinders. After CO_2 was adsorbed onto the PEI-PEG polymer layer, CO_2 reacts with amine groups in PEI, which produces $R_2NH_2^+$ and R_2NCOO^- under the acid−base reaction of R_2NH and CO_2 under electron supply, as depicted in eq 1. Additionally, the sensing performance can be enhanced via the reaction of R_2NCOO^- with CO_2 in the presence of

water molecules, as shown in eq 2. Thus, the total chemical equation can be represented by the reaction of R_2NH with CO_2 and H_2O under electron supply to form $R_2NH_2^+$ and HCO_3^-, as shown in eq 3.[45]

During the CO_2 sensing process, a current drop can be detected, as shown in the first cycle in Figure 4a; it is because the electrons were consumed, according to eq 3, in the PEI-PEG adsorption layer by the reaction between $2R_2NH$ and $3CO_2$. After the current reaches the setting point, the gases, including air and CO_2, were pumped, resulting in the current increase owing to the reverse reaction of eq 3.
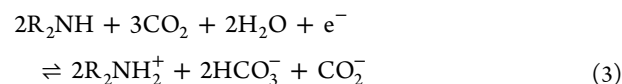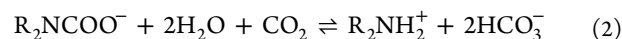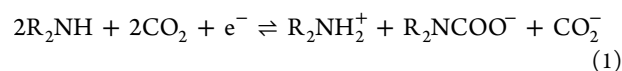
$$2R_2NH + 2CO_2 + e^- \rightleftharpoons R_2NH_2^+ + R_2NCOO^- + CO_2^- \tag{1}$$

$$R_2NCOO^- + 2H_2O + CO_2 \rightleftharpoons R_2NH_2^+ + 2HCO_3^- \tag{2}$$

$$2R_2NH + 3CO_2 + 2H_2O + e^-$$
$$\rightleftharpoons 2R_2NH_2^+ + 2HCO_3^- + CO_2^- \tag{3}$$

Figure 5a depicts the consecutive CO_2 sensing results of the PEI-PEG/ZnO/NUNCD/Si electrode, which was periodically measured under the CO_2 concentrations of 15, 12, 10, 8, 6, 4, and 2%, and the results reveal that the electrode is sensitive to CO_2 concentration under 1 atm at room temperature. Distinctly different responses can be observed in the cyclic tests from high to low CO_2 concentrations, which simulate exhalation from severe COPD patients (>13.16%), mild COPD patients (6.5−7.9%), and healthy people (4.6−5.9%). The current, with high stability without drift, indicates the
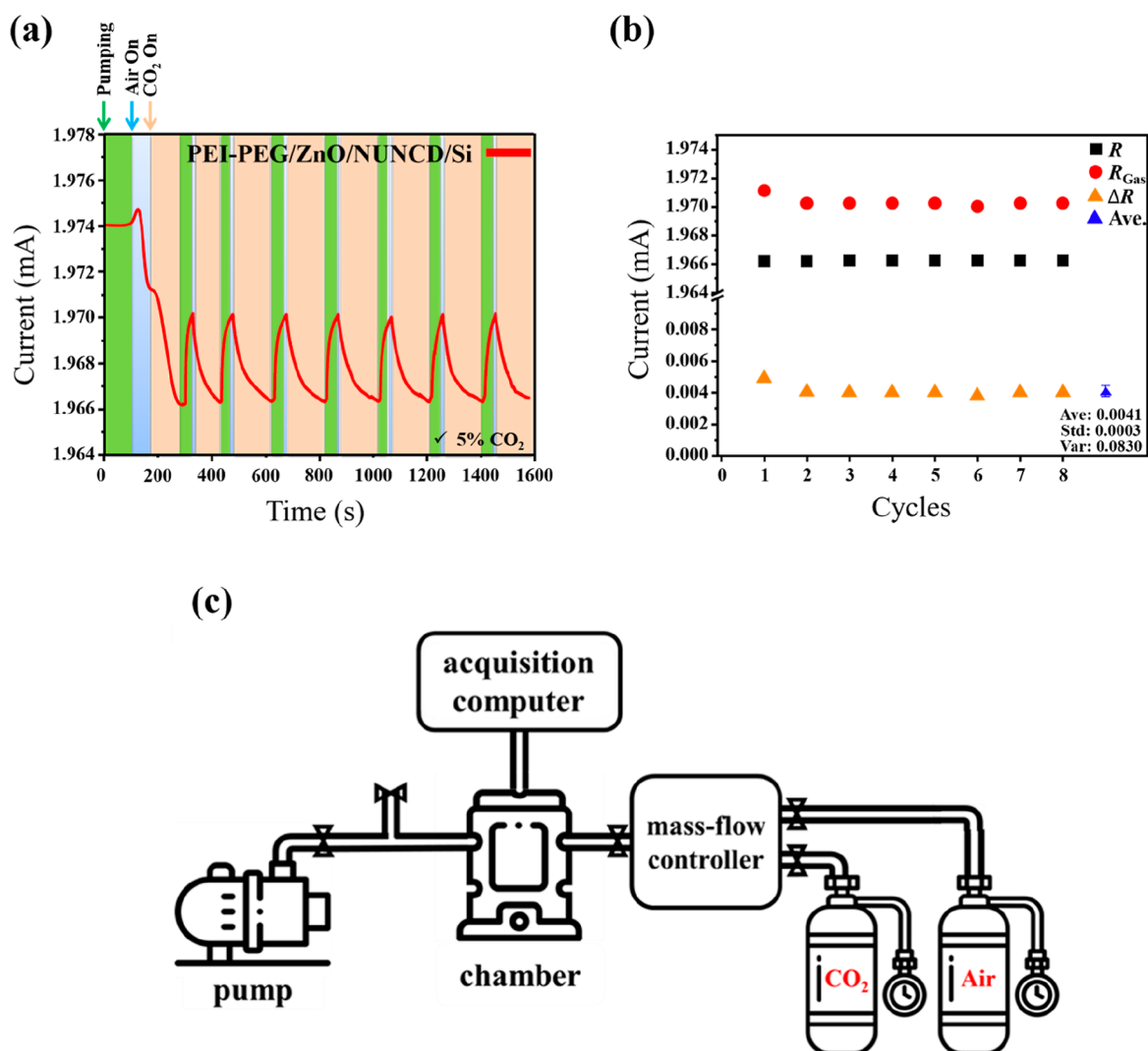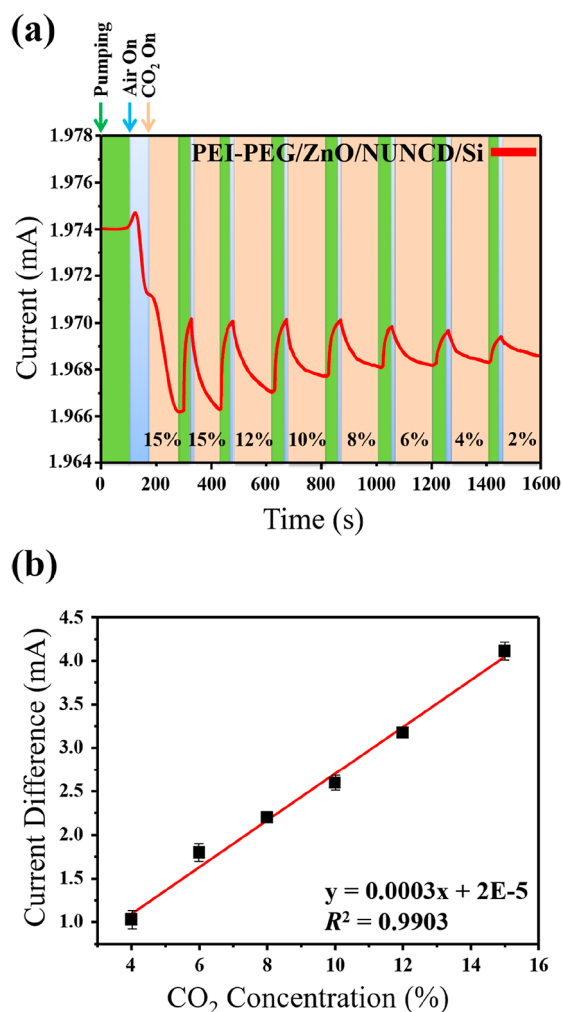
Figure 4. (a) Consecutive CO_2 gas tests of the PEI-PEG/ZnO/NUNCD/Si electrode under the same CO_2 concentration, (b) current response during cyclic tests, and (c) schematic of the measurement system.

replicability of the electrode; even after cyclic tests in an air environment, the electrode still maintained excellent stability and reversibility, which provides the convenience of easy handling for noninvasive testing.

Figure 5b shows the dependence of the current difference ΔR versus CO_2 concentration calculated based on the responses shown in Figure 5a. The current difference tended to decrease with the reduction of CO_2 concentration, corresponding to a good linear relationship with $R^2 = 0.9903$. This indicated that the response of the PEI-PEG/ZnO/NUNCD/Si electrode has excellent sensitivity, selectivity, and stability for the exhalation detection in COPD patients. Furthermore, the sensing performance of the PEI-PEG/ZnO/NUNCD/Si electrode is better than those of the PEI-PEG/NUNCD/Si and the PEI-PEG/ZnO/Si electrodes, as shown in Figure S2; without ZnO or NUNCD, the electrodes display poor sensing results on sensitivity and selectively.

To characterize the heterogeneous structure of ZnO on NUNCD/Si, FESEM, STEM, and EDS mapping were used to analyze the microstructure. Figure 6a depicts a cross-sectional view of ZnO showing a flower-like structure on the NUNCD film. The average length and diameter of the flower-like ZnO are approximately 500 and 50 nm, respectively, showing a high
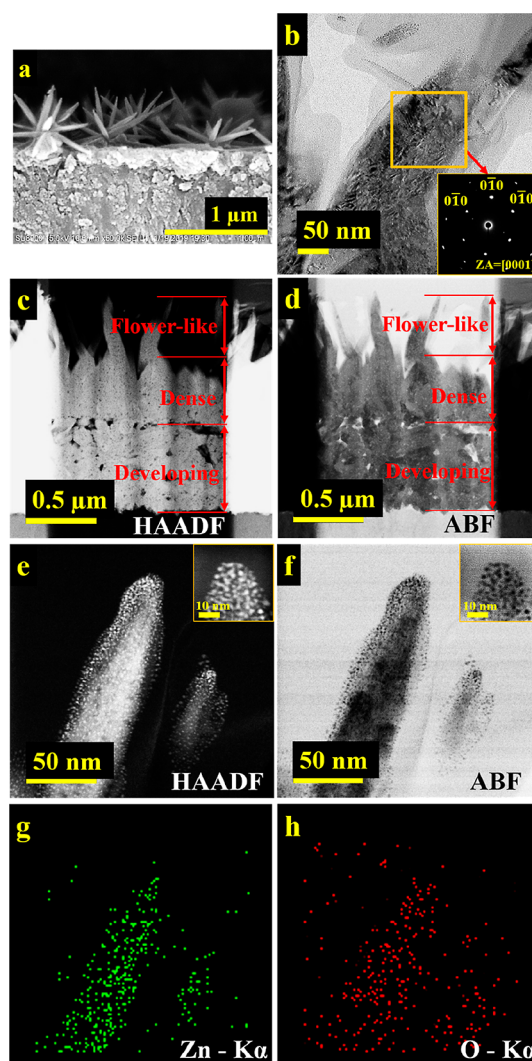
aspect ratio of 10. Figure 6b depicts the amplitude-contrast TEM micrograph of a single flower-like ZnO and the selected area electron diffraction (SAED) dot pattern, as illustrated in the inset in Figure 6b, which further demonstrates the single crystal structure of the flower-like ZnO. According to the clear SAED dot pattern of ZnO, it reveals that ZnO prefers to grow along the m-axis $[0\bar{1}0]$ as its preferred orientation (flower-like growth direction); therefore, the growth of ZnO consistently yields the {100} crystal plane as the dominant facet. Figure 6c,e shows the low magnification of the ZnO bundle and high-magnification STEM-HAADF images of a single flower-like ZnO, and Figure 6d,f shows the low-magnification ZnO bundle and high-magnification STEM-ABF mode images of a single flower-like ZnO. STEM-ABF and STEM-HAADF were used to examine light and heavy elements in the material, respectively. The contrast in Figure 6c,d clearly shows the ZnO structure, which is divided into two regions, one is in the form of a ZnO film and the other is flower-like ZnO. The thickness of the ZnO film is 1000 nm (including a 600 nm developing layer and 400 nm dense layer), and that of the flower-like structure is around 300 nm. These results suggest that ZnO growth initiates from the NUNCD film through the heterogeneous nucleation process, as a result, forming a developing ZnO layer

Figure 5. (a) Consecutive CO_2 gas tests of the PEI-PEG/ZnO/NUNCD/Si electrode under different CO_2 concentrations and (b) linear fitting of CO_2 sensing results at different CO_2 concentrations.

Figure 6. (a) SEM image, (b) TEM image with SAED pattern, (c) low-magnification STEM-HAADF image, (d) low STEM-ABF image, (e) high-magnification STEM-HAADF image, and (f) high STEM-ABF image of a cross-section of the flower-like ZnO. EDS mapping spectra of (g) Zn Kα and (h) O Kα corresponding to Figure 6e.

with a porous structure. During the growth process, decreasing the precursor concentration lowered the growth rate, leading to uniform growth of ZnO with higher crystallinity and denser structure. Thereafter, ZnO with a flower-like structure can be observed due to a slow growth rate originally from the relatively low precursor concentration. The STEM images depicted in Figure 6e,f show that a tiny nanocrystal formed on the head of the ZnO nanorod, indicating that the surface of the flower-like ZnO structure was covered by a large amount of ZnO nanoparticles, as shown in the insets of Figure 6e,f. Further characterization using EDS mapping demonstrated that the nanoparticles are composed of zinc and oxygen, as illustrated in Figure 6g,h, respectively. The tiny ZnO nanocrystals contribute to a high surface area, which can also improve the sensitivity during the sensing process.

The ultraviolet photoelectron spectrometer (UPS) spectra of ZnO/NUNCD, NUNCD, and ZnO on Si substrates are shown in Figure 7a. According to the results, the onset energies of secondary electrons for ZnO/NUNCD, NUNCD, and ZnO were estimated to be 14.5, 12.5, and 12.22 eV, respectively, and the Fermi levels were estimated to be 1.68, 0.68, and −0.01 eV, respectively. When two semiconductors with different energy gaps form a heterojunction structure, the energy gaps are reconciled at the interface, thus affecting the onset energy of

secondary electrons and the Fermi energy level.[46] Moreover, to calculate the work function, the following equation holds

$$\Phi = h\nu - (E_0 - E_f) \tag{4}$$

where Φ, h, ν, E_0, and E_f are the work function, Planck's constant, frequency of UV light, onset energy of secondary electrons, and Fermi level, respectively. Work functions of the heterojunction of the electrodes are depicted in Figure 7b.

According to the eq 4, it was found that the Φ values of ZnO/NUNCD, NUNCD, and ZnO were 8.40, 9.40, and 8.99 eV, respectively. Thus, a lower Φ represents a higher E_f, which causes a higher transition probability of the electron to the conduction band. In addition, a lower Φ can also lead to a higher current density. According to the Richardson–Dushman equation, as shown in eq 5, the relationship between the current density and work function can be correlated by

$$j_s = AT^2 \exp(-\Phi/kT) \tag{5}$$

(a)

(b)
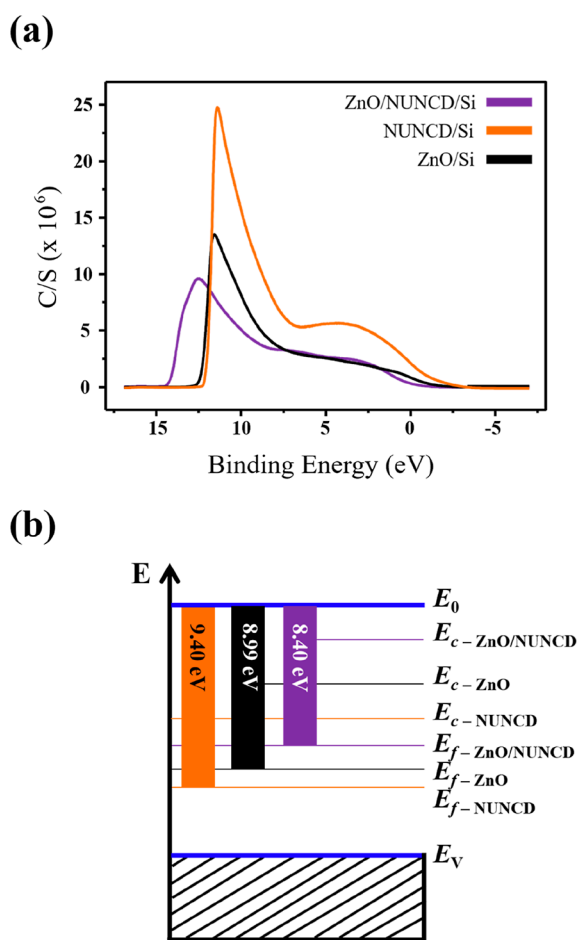
Figure 7. (a) UPS spectra and (b) band positions of ZnO/NUNCD, NUNCD, and ZnO.

where j_s is the current density of the emission, A is Richardson's constant, T is the temperature, Φ is the work function, and k is the Boltzmann constant.

Apparently, the ZnO/NUNCD heterojunction system has a better sensitivity than NUNCD and ZnO owing to its higher j_s value resulting from lower Φ, which indirectly confirms that the ZnO/NUNCD heterojunction system possesses the best sensing performance among the electrodes prepared in this work.

CONCLUSIONS

In this study, a PEI-PEG/ZnO/NUNCD/Si heterojunction CO_2 sensor was prepared showing excellent sensitivity and selectivity with easy operation at room temperature. The outstanding performance is ascribed to the high surface area of the flower-like ZnO and the low work function of the ZnO/NUNCD heterojunction structure, generating high active sites and high current densities, respectively. The ZnO nanoparticles formed on the tip of the flower-like ZnO provide an additional active adsorption area. Furthermore, the selectivity was attributed to the PEI-PEG polymer, even in the presence of atmospheric gases such as O_2, N_2, and Ar. All these factors lead to the high sensitivity and selectivity of the PEI-PEG/ZnO/NUNCD/Si heterojunction structure.

The PEI-PEG/ZnO/NUNCD/Si heterojunction structure showing exceptional high performance on practical CO_2 sensing at room temperature is demonstrated. The in-depth investigation of the sensing mechanism reveals that the heterojunction structure indeed promotes sensitivity, and the PEI-PEG blend enhances the selectivity of the sensor. The promising results obtained in this study are favorable for the applications such as CO_2 sensors, which will assist in developing COPD biosensors for in vitro CO_2 sensing. These results indicate that the PEI-PEG/ZnO/NUNCD/Si heterojunction electrode has great potential for use in noninvasive sensors as an alternative device to alleviate discomfort during invasive medical procedures, especially for COPD patients.

ASSOCIATED CONTENT

Ⓢ Supporting Information

The Supporting Information is available free of charge at https://pubs.acs.org/doi/10.1021/acsomega.2c00479.

FESEM image of ZnO/Si without NUNCD; and CO_2 sensing behaviors of PEI-PEG/NUNCD/Si and PEI-PEG/ZnO/Si electrodes (PDF)

AUTHOR INFORMATION

Corresponding Author

Nyan-Hwa Tai − *Department of Materials Science and Engineering, National Tsing-Hua University, Hsinchu 30013, Taiwan;* ⓞ orcid.org/0000-0003-4755-1398; Phone: +886 5715131 (#31026); Email: nhtai@mx.nthu.edu.tw

Authors

Ching Chang − *Department of Materials Science and Engineering, National Tsing-Hua University, Hsinchu 30013, Taiwan*

Chi-Young Lee − *Department of Materials Science and Engineering, National Tsing-Hua University, Hsinchu 30013, Taiwan*

Complete contact information is available at:
https://pubs.acs.org/10.1021/acsomega.2c00479

Author Contributions

C.C.: idea initiation, designing and carrying out the experiment, data acquisition and analyses, and manuscript preparation. C.-Y.L.: co-advisor, discussion on the weekly progress report. N.-H.T.: advisor, idea approval, instruction on research progress, and discussion on the manuscript preparation.

Notes

The authors declare no competing financial interest.

REFERENCES

(1) Gangwar, R. K.; Dhumale, V. A.; Date, K. S.; Alegaonkar, P.; Sharma, R. B.; Datar, S. Decoration of gold nanoparticles on thin multiwall carbon nanotubes and their use as a glucose sensor. *Mater. Res. Express* **2016**, *3*, 035008.

(2) Chinke, S. L.; Berhe, S.; Alegaonkar, P. S. High Speed Projectile Sensor: Design, Development and System Engineering. *IEEE Sens. J.* **2021**, *21*, 27062−27068.

(3) Godbole, R. V.; Rao, P.; Alegaonkar, P. S.; Bhagwat, S. Influence of fuel to oxidizer ratio on LPG sensing performance of $MgFe_2O_4$ nanoparticles. *Mater. Chem. Phys.* **2015**, *161*, 135−141.

(4) Gautam, S.; Kumar, D.; Alegaonkar, P. S.; Jha, P.; Jain, N.; Rawat, J. S. Enhanced response and improved selectivity for toxic gases with functionalized CNT thin film resistors. *Integr. Ferroelectr.* **2018**, *186*, 65−70.

(5) Ugale, A. D.; Jagtap, R. V.; Pawar, D.; Datar, S.; Kale, S. N.; Alegaonkar, P. S. Nano-carbon: Preparation, assessment, and applications for NH_3 gas sensor and electromagnetic interference shielding. *RSC Adv.* **2016**, *6*, 97266−97275.

(6) Godbole, R.; Godbole, V. P.; Alegaonkar, P. S.; Bhagwat, S. Effect of film thickness on gas sensing properties of sprayed WO_3 thin films. *New J. Chem.* **2017**, *41*, 11807−11816.

(7) Prasad, B. Chronic Obstructive Pulmonary Disease (COPD). *Int. J. Pharm. Res. Technol.* **2020**, *10*, 67−71.

(8) Pauwels, R. A.; Buist, A. S.; Calverley, P. M. A.; Jenkins, C. R.; Hurd, S. S. Global strategy for the diagnosis, management, and prevention of chronic obstructive pulmonary disease: NHLBI/WHO Global Initiative for Chronic Obstructive Lung Disease (GOLD) Workshop summary. *Am. J. Respir. Crit. Care Med.* **2001**, *163*, 1256−1276.

(9) Nathell, L.; Nathell, M.; Malmberg, P.; Larsson, K. COPD diagnosis related to different guidelines and spirometry techniques. *Respir. Res.* **2007**, *8*, 89.

(10) Rovina, N.; Koutsoukou, A.; Koulouris, N. G. Inflammation and immune response in COPD: where do we stand? *Mediat. Inflamm.* **2013**, *2013*, 1.

(11) Kirkham, P. A.; Barnes, P. J. Oxidative stress in COPD. *Chest* **2013**, *144*, 266−273.

(12) Su, Y.; Chen, G.; Chen, C.; Gong, Q.; Xie, G.; Yao, M.; Tai, H.; Jiang, Y.; Chen, J. Self-Powered Respiration Monitoring Enabled By a Triboelectric Nanogenerator. *Adv. Mater.* **2021**, *33*, 2101262.

(13) Bongard, F.; Wu, Y.; Lee, T. S.; Klein, S. Capnographic monitoring of extubated postoperative patients. *J. Invest. Surg.* **1994**, *7*, 259−264.

(14) Lenz, G.; Heipertz, W.; Epple, E. Capnometry for continuous postoperative monitoring of nonintubated, spontaneously breathing patients. *J. Clin. Monit.* **1991**, *7*, 245−248.

(15) Liu, S.-Y.; Lee, T.-S.; Bongard, F. Accuracy of capnography in nonintubated surgical patients. *Chest* **1992**, *102*, 1512−1515.

(16) Mehta, J. H.; Williams, G. W.; Harvey, B. C.; Grewal, N. K.; George, E. E. The relationship between minute ventilation and end tidal CO_2 in intubated and spontaneously breathing patients undergoing procedural sedation. *PLoS One* **2017**, *12*, No. e0180187.

(17) Ellis, J. E.; Star, A. Carbon nanotube based gas sensors toward breath analysis. *ChemPlusChem* **2016**, *81*, 1248.

(18) Liao, B.; Wei, Q.; Wang, K.; Liu, Y. Study on $CuO−BaTiO_3$ semiconductor CO_2 sensor. *Sens. Actuators, B* **2001**, *80*, 208−214.

(19) Jinesh, K. B.; Dam, V. A. T.; Swerts, J.; de Nooijer, C.; van Elshocht, S.; Brongersma, S. H.; Crego-Calama, M. Room-temperature CO_2 sensing using metal−insulator−semiconductor capacitors comprising atomic-layer-deposited La_2O_3 thin films. *Sens. Actuators, B* **2011**, *156*, 276−282.

(20) Chen, X.; Zhu, H.; Cai, J.; Wu, Z. High-performance 4H-SiC-based ultraviolet p-i-n photodetector. *J. Appl. Phys.* **2007**, *102*, 024505.

(21) Al-Hardan, N. H.; Jalar, A.; Hamid, M. A.; Keng, L. K.; Ahmed, N. M.; Shamsudin, R. A wide-band UV photodiode based on n-ZnO/p-Si heterojunctions. *Sens. Actuators, A* **2014**, *207*, 61−66.

(22) Liu, Z.; Liu, C.; Ya, J.; Lei, E. Controlled synthesis of ZnO and TiO_2 nanotubes by chemical method and their application in dye-sensitized solar cells. *Renewable Energy* **2011**, *36*, 1177−1181.

(23) Liu, Z.; Cai, Q.; Ma, C.; Zhang, J.; Liu, J. Photoelectrochemical properties and growth mechanism of varied ZnO nanostructures. *New J. Chem.* **2017**, *41*, 7947−7952.

(24) Hu, J.; Liu, X. W.; Pan, B. C. A study of the size-dependent elastic properties of ZnO nanowires and nanotubes. *Nanotechnology* **2008**, *19*, 285710.

(25) Lin, J.-C.; Huang, B.-R.; Lin, T.-C. Bilayer structure of ZnO nanorod/nanodiamond film based ultraviolet photodetectors. *J. Electrochem. Soc.* **2013**, *160*, H509.

(26) Dhahri, R.; Hjiri, M.; El Mir, L.; Fazio, E.; Neri, F.; Barreca, F.; Donato, N.; Bonavita, A.; Leonardi, S. G.; Neri, G. ZnO: Ca nanopowders with enhanced CO_2 sensing properties. *J. Phys. D: Appl. Phys.* **2015**, *48*, 255503.

(27) Su, Y.; Yao, M.; Xie, G.; Pan, H.; Yuan, H.; Yang, M.; Tai, H.; Du, X.; Jiang, Y. Improving sensitivity of self-powered room temperature NO_2 sensor by triboelectric-photoelectric coupling effect. *Appl. Phys. Lett.* **2019**, *115*, 073504.

(28) Su, Y.; Xie, G.; Tai, H.; Li, S.; Yang, B.; Wang, S.; Zhang, Q.; Du, H.; Zhang, H.; Du, X.; Jiang, Y. Self-powered room temperature NO_2 detection driven by triboelectric nanogenerator under UV illumination. *Nano Energy* **2018**, *47*, 316−324.

(29) Wang, S.; Jiang, Y.; Tai, H.; Liu, B.; Duan, Z.; Yuan, Z.; Pan, H.; Xie, G.; Du, X.; Su, Y. An integrated flexible self-powered wearable respiration sensor. *Nano Energy* **2019**, *63*, 103829.

(30) Nguyen, D. D.; Hsieh, P.-Y.; Tsai, M.-T.; Lee, C.-Y.; Tai, N.-H.; To, B. D.; Vu, D. T.; Hsu, C. C. Hollow few-layer graphene-based structures from parafilm waste for flexible transparent supercapacitors and oil spill cleanup. *ACS Appl. Mater. Interfaces* **2017**, *9*, 40645−40654.

(31) Sankaran, K. J.; Huang, B.-R.; Saravanan, A.; Manoharan, D.; Tai, N.-H.; Lin, I.-N. Nitrogen Incorporated Ultrananocrystalline Diamond Microstructures From Bias-Enhanced Microwave N_2/CH_4-Plasma Chemical Vapor Deposition. *Plasma Process. Polym.* **2016**, *13*, 419−428.

(32) Sankaran, K. J.; Kurian, J.; Chen, H. C.; Dong, C. L.; Lee, C. Y.; Tai, N. H.; Lin, I. N. Origin of a needle-like granular structure for ultrananocrystalline diamond films grown in a N_2/CH_4 plasma. *J. Phys. D: Appl. Phys.* **2012**, *45*, 365303.

(33) Saravanan, A.; Huang, B.-R.; Sankaran, K. J.; Tai, N.-H.; Lin, I.-N. Highly conductive diamond−graphite nanohybrid films with enhanced electron field emission and microplasma illumination properties. *ACS Appl. Mater. Interfaces* **2015**, *7*, 14035−14042.

(34) Jiang, P.-L.; Hsieh, P.-Y.; Chen, Y.-C.; Lee, C.-Y.; Chang, H.-Y.; Tai, N.-H. Nitrogen-Incorporated Ultrananocrystalline Diamond Electrodes for Dopamine Determination. *J. Biomed. Nanotechnol.* **2018**, *14*, 1627−1634.

(35) Shalini, J.; Sankaran, K. J.; Lee, C.-Y.; Tai, N.-H.; Lin, I.-N. An amperometric urea bisosensor based on covalent immobilization of urease on N_2 incorporated diamond nanowire electrode. *Biosens. Bioelectron.* **2014**, *56*, 64−70.

(36) Chang, C.; Lee, C.-Y.; Tai, N.-H. Nitrogen-Incorporated Ovoid-Shaped Nanodiamond Films for Dopamine Detection. *ACS Appl. Nano Mater.* **2020**, *3*, 11970.

(37) Ouyang, W.; Teng, F.; He, J.-H.; Fang, X. Enhancing the photoelectric performance of photodetectors based on metal oxide semiconductors by charge-carrier engineering. *Adv. Funct. Mater.* **2019**, *29*, 1807672.

(38) Kahn, A. Fermi level, work function and vacuum level. *Mater. Horiz.* **2016**, *3*, 7−10.

(39) Seok, H.-J.; Ali, A.; Seo, J. H.; Lee, H. H.; Jung, N.-E.; Yi, Y.; Kim, H.-K. Zno: Ga-graded ITO electrodes to control interface between PCBM and ITO in planar perovskite solar cells. *Sci. Technol. Adv. Mater.* **2019**, *20*, 389−400.

(40) Yang, M.; Au, C.; Deng, G.; Mathur, S.; Huang, Q.; Luo, X.; Xie, G.; Tai, H.; Jiang, Y.; Chen, C.; Cui, Z.; Liu, X.; He, C.; Su, Y.; Chen, J. $NiWO_4$ Microflowers on Multi-Walled Carbon Nanotubes for High-Performance NH_3 Detection. *ACS Appl. Mater. Interfaces* **2021**, *13*, 52850−52860.

(41) Lin, C.-C.; Gupta, S.; Chang, C.; Lee, C.-Y.; Tai, N.-H. Polyethylenimine-polyethylene glycol/multi-walled carbon nanotubes bilayer structure for carbon dioxide gas sensing at room temperature. *Mater. Lett.* **2021**, *297*, 129941.

(42) Paskal, A.; Paskal, W.; Pietruski, P.; Wlodarski, P. Polyethylene glycol: the future of posttraumatic nerve repair? Systemic review. *Int. J. Mol. Sci.* **2019**, *20*, 1478.

(43) Liu, B.; Libanori, A.; Zhou, Y.; Xiao, X.; Xie, G.; Zhao, X.; Su, Y.; Wang, S.; Yuan, Z.; Duan, Z. Simultaneous Biomechanical and

Biochemical Monitoring for Self-Powered Breath Analysis. *ACS Appl. Mater. Interfaces* **2022**, *14*, 7301.

(44) Sakwa-Novak, M. A.; Tan, S.; Jones, C. W. Role of additives in composite PEI/oxide CO_2 adsorbents: enhancement in the amine efficiency of supported PEI by PEG in CO_2 capture from simulated ambient air. *ACS Appl. Mater. Interfaces* **2015**, *7*, 24748−24759.

(45) Xie, W.; Yu, M.; Wang, R. CO_2 capture behaviors of amine-modified resorcinol-based carbon aerogels adsorbents. *Aerosol Air Qual. Res.* **2017**, *17*, 2715−2725.

(46) Zhong, Y.; Peng, C.; He, Z.; Chen, D.; Jia, H.; Zhang, J.; Ding, H.; Wu, X. Interface engineering of heterojunction photocatalysts based on 1D nanomaterials. *Catal. Sci. Technol.* **2021**, *11*, 27−42.